J Mater Sci (2020) 55:9748–9761

Advanced Nano Materials

Co-precipitation synthesized nanostructured $Ce_{0.9}Ln_{0.05}Ag_{0.05}O_{2-\delta}$ materials for solar thermochemical conversion of CO_2 into fuels

Gorakshnath Takalkar[1], Rahul R. Bhosale[1,*], Fares AlMomani[1], and Suliman Rashid[1]

[1] *Department of Chemical Engineering, College of Engineering, Qatar University, P. O. Box 2713, Doha, Qatar*

Received: 14 January 2020
Accepted: 13 March 2020
Published online: 27 March 2020

ABSTRACT

Synthesis, characterization, and application of $Ce_{0.9}Ln_{0.05}Ag_{0.05}O_{2-\delta}$ materials (where, Ln = La, Pr, Nd, Sm, Gd, Tb, Dy, Er) for the thermochemical conversion of CO_2 reported in this paper. The $Ce_{0.9}Ln_{0.05}Ag_{0.05}O_{2-\delta}$ materials were synthesized by using an ammonium hydroxide-driven co-precipitation method. The derived $Ce_{0.9}Ln_{0.05}Ag_{0.05}O_{2-\delta}$ materials were characterized via powder X-ray diffraction, scanning electron microscope, and electron diffraction spectroscopy. The characterization results indicate the formation of spherically shaped $Ce_{0.9}Ln_{0.05}Ag_{0.05}O_{2-\delta}$ nanostructured particles. As-prepared $Ce_{0.9}Ln_{0.05}Ag_{0.05}O_{2-\delta}$ materials were further tested toward multiple CO_2 splitting cycles by utilizing a thermogravimetric analyzer. The results obtained indicate that all the $Ce_{0.9}Ln_{0.05}Ag_{0.05}O_{2-\delta}$ materials produced higher quantities of O_2 and CO than the previously studied pure CeO_2 and lanthanide-doped ceria materials. Overall, the $Ce_{0.911}La_{0.053}Ag_{0.047}O_{1.925}$ showed the maximum redox reactivity in terms of O_2 release (72.2 μmol/g cycle) and CO production (136.6 μmol/g cycle).

List of symbols

n_{O_2}	Moles of O_2 (μmol/g)
n_{CO}	Moles of CO (μmol/g)
Δm_{loss}	Amount of loss in the mass (mg)
Δm_{gain}	Amount of gain in the mass (mg)
M_{O_2}	Molecular weight of O_2 (g/mol)
M_O	Molecular weight of O (g/mol)
$m_{Ce_{0.9}Ln_{0.05}Ag_{0.05}O_{2-\delta}}$	Mass of the $Ce_{0.9}Ln_{0.05}Ag_{0.05}O_{2-\delta}$ materials (mg)

Introduction

The worldwide human population is rising at a quick pace, which inherently demands a large amount of energy for consumption [1]. Current energy production largely depends on the utilization of fossil fuels. The excessive use of petroleum-based resources results in a continuous CO_2 discharge [2, 3]. This constant release of CO_2 is considered as one of the

Address correspondence to E-mail: rahul.bhosale@qu.edu.qa; rrbhosle@yahoo.com

https://doi.org/10.1007/s10853-020-04567-w

primary reasons for the variation in the climate parameters [4]. The environmental distress occurring due to increases in CO_2 emission generated more interest in the conversion of CO_2 into value-added products.

One of the possible options for CO_2 utilization is to convert the captured CO_2 into fuels. Solar thermochemical cycles driven based on the metal oxide (MO)-based redox reactions can split CO_2 into CO (Fig. 1) [5, 6]. The solar CO produced can be combined with the solar H_2 (produced via solar thermochemical splitting of water) for the manufacturing of the solar syngas, which can be further utilized in the catalytic Fischer–Tropsch process [7].

The MO-based solar-driven thermochemical conversion of CO_2 is a two-phase process. In the first phase, the MO is reduced with the help of concentrated solar power, and in phase 2, the reduced MO is re-oxidized again via a CO_2 splitting reaction. Zinc oxide [8, 9], tin oxide [10, 11], iron oxide [12, 13], CeO_2 [14–16], doped ceria [17–20], ferrites [21–24], perovskites [25–28], and others [29–32] have been utilized for the solar thermochemical conversion of H_2O and CO_2. Among all these, the phase pure CeO_2 is considered as one of the promising options due to its faster reaction kinetics and better thermal stability. Although the CeO_2 is beneficial for the thermochemical conversion of H_2O and CO_2, a lower fuel production capacity is one of the major limitations associated with this MO.

Recently, Bhosale and Takalkar [33] reported that the doping of lanthanides such as La, Pr, Nd, Sm, Gd, Tb, Dy, and Er into CeO_2 fluorite cubic crystal structure improved the thermal reduction (TR) capacity of the CeO_2. It was also reported that although the TR capability of CeO_2 was improved, only $Ce_{0.9}La_{0.1}O_2$ was capable of producing higher quantities of CO than CeO_2 via CO_2 splitting reaction. In another investigation, Takalkar et al. [19] reported that the inclusion of Ag in the transition metal-doped ceria considerably improved the TR as well as CO_2 splitting (CDS) capacity.

Based on the results reported in our previous investigations, in this study, the synthesis, characterization, and application of $Ce_{0.9}Ln_{0.05}Ag_{0.05}O_{2-\delta}$ materials (where, Ln = La, Pr, Nd, Sm, Gd, Tb, Dy, Er) for the thermochemical conversion of CO_2 is reported. Synthesis of the $Ce_{0.9}Ln_{0.05}Ag_{0.05}O_{2-\delta}$ materials is achieved via a co-precipitation method. The derived materials are further tested for multiple thermochemical CDS cycles by utilizing a thermogravimetric analyzer (TGA) setup. The TR and CDS capacity of the $Ce_{0.9}Ln_{0.05}Ag_{0.05}O_{2-\delta}$ materials was estimated and compared with the previously studied phase pure CeO_2 and lanthanide-doped ceria materials.

Experimental

Preparation and characterization of $Ce_{0.9}Ln_{0.05}Ag_{0.05}O_{2-\delta}$

Nitrate-based precursors of ceria, silver, and all lanthanides were acquired from Sigma-Aldrich, USA.

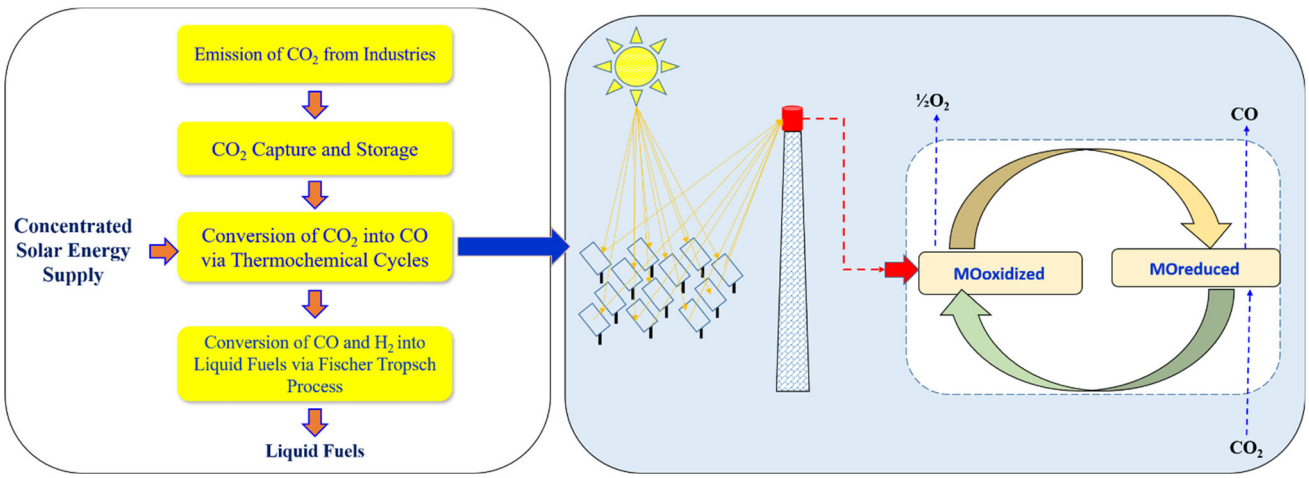

Figure 1 Overall process of production of liquid fuels by using solar syngas generated via MO-based solar thermochemical H_2O/CO_2 splitting cycle.

Aqueous 28% NH_3OH as a precipitating agent was procured from the same supplier. Ultrapure deionized (DI) water (produced through Direct-Q system, Millipore, France) was utilized for the preparation of nitrate solution. An ultrapure grade Ar gas (purity 99.999%) and 50% CO_2 + 50% Ar gas mixture are ordered from the Buzwair Scientific and Technical Gases, Doha, Qatar.

The synthesis of redox $Ce_{0.9}Ln_{0.05}Ag_{0.05}O_{2-\delta}$ materials was achieved via co-precipitation of the hydroxide method. As shown in Fig. 2, an aqueous mixture of selected metal precursors was prepared by dissolving them in 300 ml of deionized water. To this mixture, aqueous ammonium hydroxide (28%) was added to attain a pH approximately equal to 10. The mixture further stirred for 24 h with a maintained pH ~ 10. Once the stirring was stopped, the precipitate of $Ce_{0.9}Ln_{0.05}Ag_{0.05}O_{2-\delta}$ material was allowed to settle via gravity (mixture kept undisturbed overnight). The next morning, the supernatant liquid was decanted, and the obtained precipitate was washed several times by deionized water with the help of a vacuum filtration unit. The obtained filtered cake of $Ce_{0.9}Ln_{0.05}Ag_{0.05}O_{2-\delta}$ was dried (120 °C, 5 h), crushed, and annealed (Nabertherm Furnace) up to 1000 °C for 4 h in the presence of air. The obtained annealed powder was analyzed for the determination of the phase/elemental composition and morphology by using Panalytical XPert powder X-ray diffractometer (PXRD) and scanning electron microscope (SEM, Nova Nano 450, FEI) equipped with the electron diffraction spectroscopy (EDS).

CO_2 splitting experiments

The $Ce_{0.9}Ln_{0.05}Ag_{0.05}O_{2-\delta}$ materials were experimentally tested in a TGA setup (Setaram Instrumentation, France), which is shown in Fig. 3. The experimental parameters utilized to perform the thermochemical cycles are given in Table 1. Approximately, 50 mg of the calcined $Ce_{0.9}Ln_{0.05}Ag_{0.05}O_{2-\delta}$ powder was charged in an alumina (100 µl) crucible, and then placed inside the heating furnace of the TGA. Before performing the TGA experiments, the residual air filling the hollow space near to the furnace was evacuated by applying a vacuum followed by sweeping by the inert Ar. Chilled water (generated by Julabo FC 1600T) was utilized to decrease the exiting gas stream temperature. Additional details related to the TGA setup and the experimental procedure are already described in our previous studies [23, 29]. Multiple TR and CDS steps were performed by considering the operating parameters given in Table 1.

The mass variations allied with the $Ce_{0.9}Ln_{0.05}Ag_{0.05}O_{2-\delta}$ materials during the TR and CDS steps were documented after subtracting the blank TGA experimental data from the actual TGA experimental

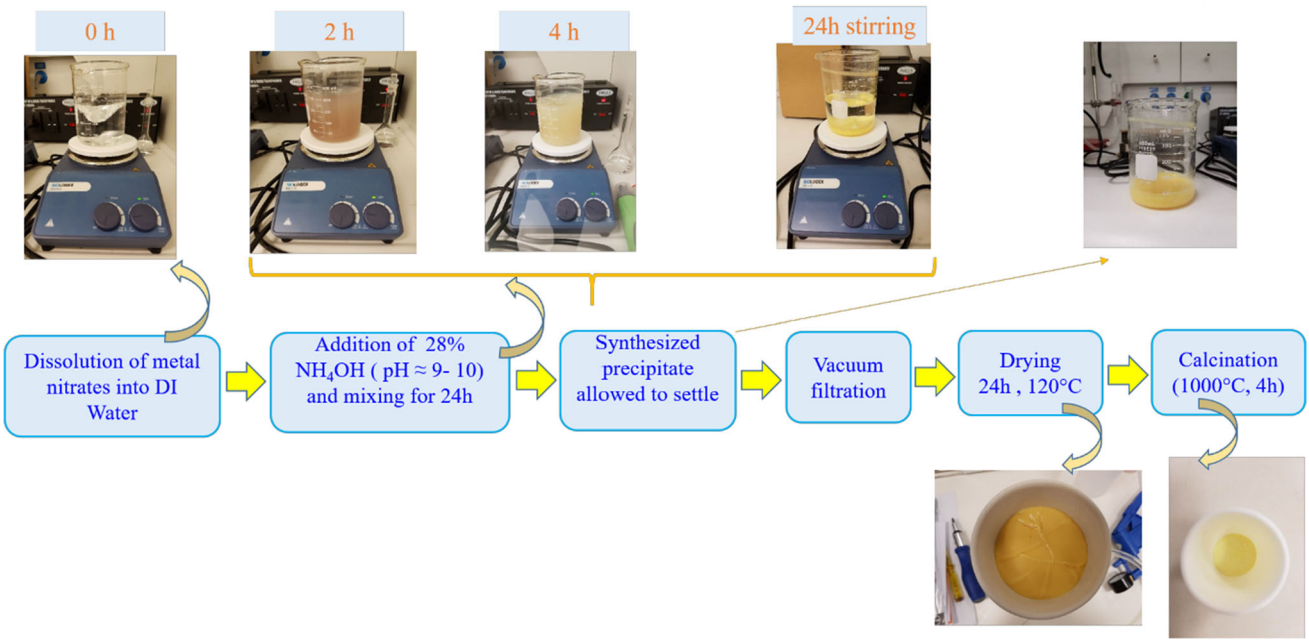

Figure 2 Synthesis of $Ce_{0.9}Ln_{0.05}Ag_{0.05}O_{2-\delta}$ materials via the co-precipitation method.

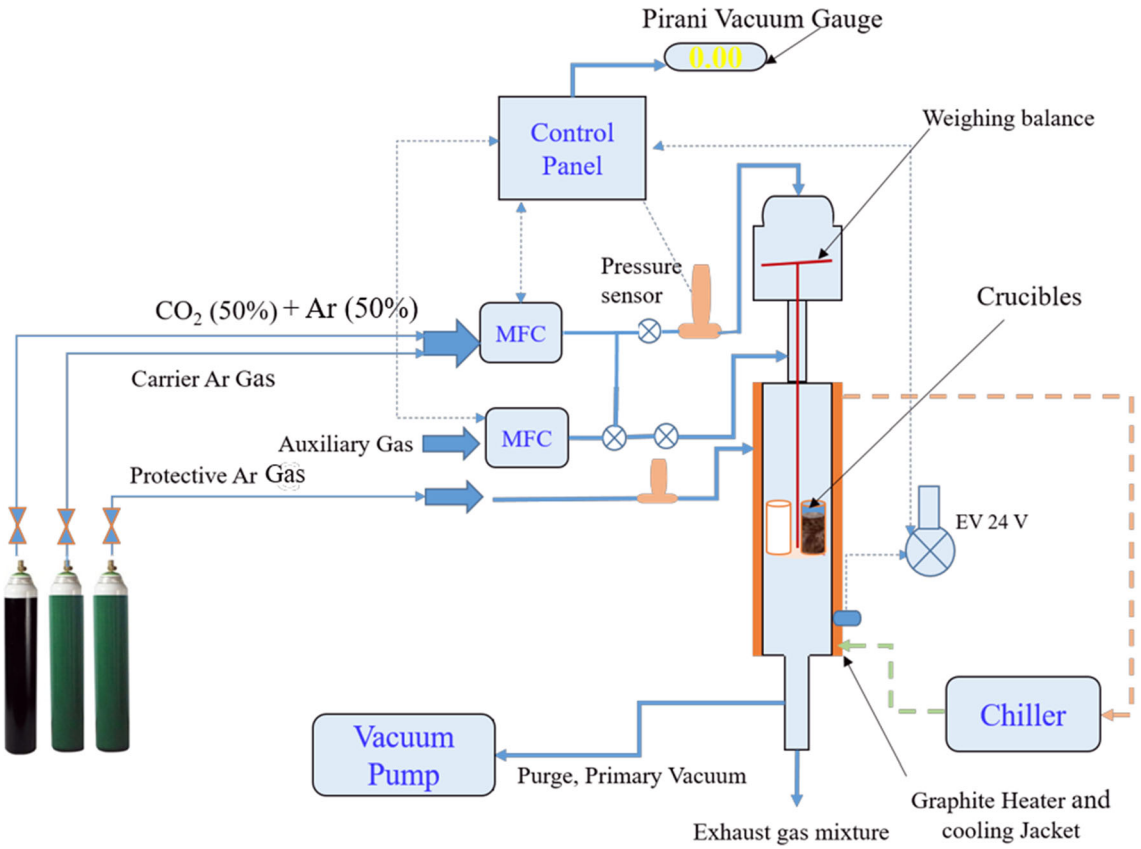

Figure 3 TGA experimental setup.

Table 1 Experimental conditions used for the TGA experiments

Parameters	Value
Carrier gas	Ultrapure inert Ar
Feed gas mixture	50% CO_2 + 50% Ar
Flowrate of carrier and feed gas mixture	100 ml/min
TR and CDS temperature	1400 °C and 1000 °C
Heating and cooling rate	25 K/min
Reaction time for TR and CDS	60 min and 30 min

data. The amount of O_2 liberated (μmol/g) during the TR step and the quantity of CO produced during the CDS step are calculated by utilizing Eqs. (1) and (2).

$$n_{O_2} = \frac{\Delta m_{\text{loss}}}{\left(M_{O_2} \times m_{Ce_{0.9}Ln_{0.05}Ag_{0.05}O_{2-\delta}}\right)} \quad (1)$$

$$n_{CO} = \frac{\Delta m_{gain}}{\left(M_{O} \times m_{Ce_{0.9}Ln_{0.05}Ag_{0.05}O_{2-\delta}}\right)} \quad (2)$$

Results and discussion

After synthesizing the $Ce_{0.9}Ln_{0.05}Ag_{0.05}O_{2-\delta}$ materials, the next important step was to determine the phase composition of the derived materials. PXRD profiles of the calcined $Ce_{0.9}Ln_{0.05}Ag_{0.05}O_{2-\delta}$ materials are shown in Fig. 4a, b. The presented patterns indicate a cubic fluorite crystal structure of the $Ce_{0.9}Ln_{0.05}Ag_{0.05}O_{2-\delta}$ materials, similar to the one reported in the case of CeO_2 [23]. The PXRD profiles shown in Fig. 4a further indicates the absence of the formation of any metal or metal oxide impurities. As shown in Fig. 4b, the $Ce_{0.9}Ln_{0.05}Ag_{0.05}O_{2-\delta}$ material peaks shift toward either lower or higher 2θ angle (based on the crystal ionic radii of the dopants). This shift in the peaks further confirmed the successful incorporation of the dopants inside the ceria fluorite crystal structure. The formation of nominally phase pure $Ce_{0.9}Ln_{0.05}Ag_{0.05}O_{2-\delta}$ materials was also assured via EDS analysis (results given in Table 2).

In order to determine the crystallite size, a widely used Scherrer equation and the PXRD data associated with the $Ce_{0.9}Ln_{0.05}Ag_{0.05}O_{2-\delta}$ materials were utilized.

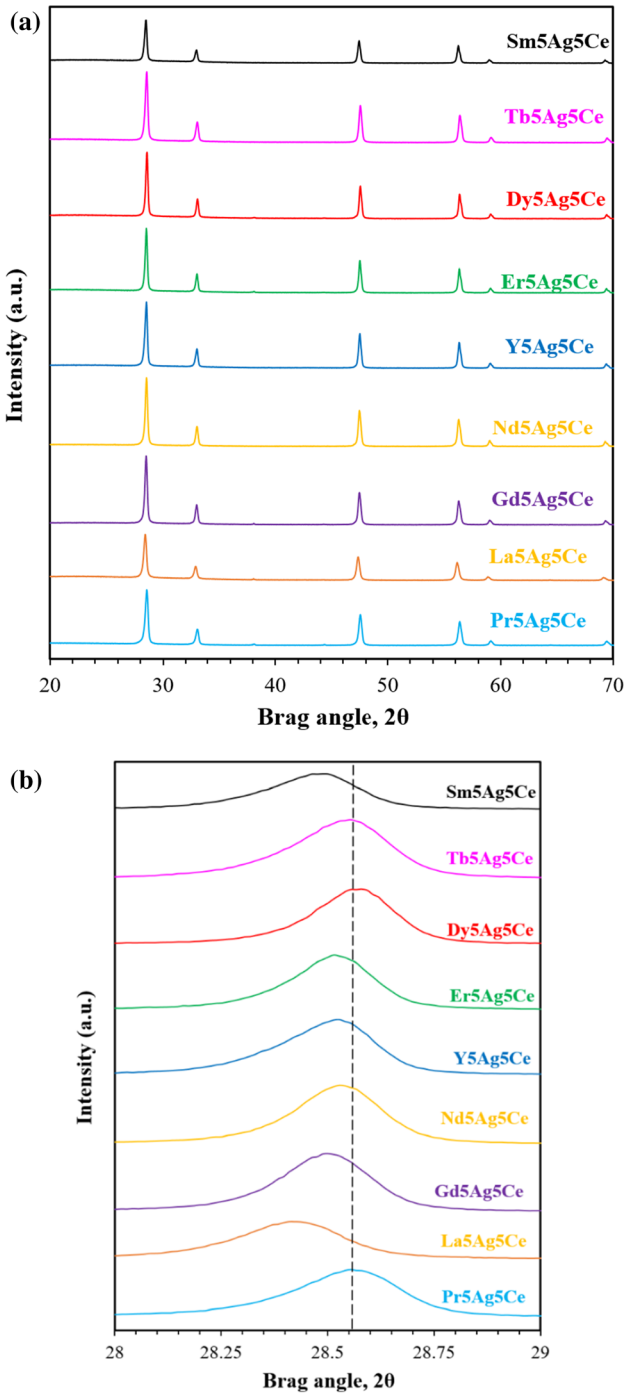

Figure 4 PXRD patterns of the $Ce_{0.9}Ln_{0.05}Ag_{0.05}O_{2-\delta}$ materials.

Table 2 indicates that the variation in the crystallite size of the $Ce_{0.9}Ln_{0.05}Ag_{0.05}O_{2-\delta}$ materials does not follow any specific trend. As per the obtained results, the $Ce_{0.9}Ln_{0.05}Ag_{0.05}O_{2-\delta}$ materials can be arranged as follows based on their average crystallite size: La_5Ag_5Ce > Dy_5Ag_5Ce > Sm_5Ag_5Ce > Pr_5Ag_5Ce > Tb_5Ag_5Ce > Gd_5Ag_5Ce > Er_5Ag_5 Ce > Nd_5Ag_5Ce.

After estimating the composition and crystallite size of each $Ce_{0.9}Ln_{0.05}Ag_{0.05}O_{2-\delta}$ material, the morphology was scrutinized by performing the SEM analysis. The SEM images obtained looks very similar to each other and indicate the formation of roughly spherical particles of $Ce_{0.9}Ln_{0.05}Ag_{0.05}O_{2-\delta}$. The microscopic SEM analysis further confirmed that the particles were agglomerated. It was also observed that the average particle size was very close to the crystallite sizes given in Table 2. The representative SEM images of Pr_5Ag_5Ce, Tb_5Ag_5Ce, Gd_5Ag_5Ce, and Er_5Ag_5Ce are shown in Fig. 5.

The redox performance of the $Ce_{0.9}Ln_{0.05}Ag_{0.05}O_{2-\delta}$ materials is estimated by performing the thermochemical CDS experiments using the TGA setup. $Ce_{0.9}Ln_{0.05}Ag_{0.05}O_{2-\delta}$ materials thermally reduced at 1400 °C (10 K/min) for 60 min in the presence of the inert Ar (100 ml/min) and then re-oxidized at 1000 °C by using a feed gas mixture containing 50% CO_2 + 50% Ar (100 ml/min). As an example, Fig. 6 represents a TGA profile of La_5Ag_5Ce material obtained during the first CDS cycle. As shown in Fig. 6, during the TR step, the mass of the La_5Ag_5Ce material reduced by 0.511 mg, and during the CDS step, the weight of the La_5Ag_5Ce material increased by 0.126 mg. These mass variations further converted into respective redox performances in terms of n_{O_2} released (320.2 µmol/g) and n_{CO} produced (157.8 µmol/g) by using Eqs. (1) and (2).

The mass variations associated with the $Ce_{0.9}Ln_{0.05}Ag_{0.05}O_{2-\delta}$ materials recorded during the first cycle are shown in Fig. 7a, b. The n_{O_2} released and n_{CO} produced by each $Ce_{0.9}Ln_{0.05}Ag_{0.05}O_{2-\delta}$ material was computed based on the obtained TGA profiles and given in Table 3. The data given in Table 3 show that the Pr_5Ag_5Ce was capable of releasing a higher amount of O_2 at 1400 °C than the other $Ce_{0.9}Ln_{0.05}Ag_{0.05}O_{2-\delta}$ materials. Likewise, the CO production aptitude of La_5Ag_5Ce was the uppermost when compared with the remaining $Ce_{0.9}Ln_{0.05}Ag_{0.05}O_{2-\delta}$ materials. The numbers listed in the n_{CO}/n_{O_2} ratio column shows that the re-oxidation ability of the

Table 2 Abbreviations, chemical composition, crystallite size, and cell parameter of each $Ce_{0.9}Ln_{0.05}Ag_{0.05}O_{2-\delta}$ material

Abbreviations	$Ce_{0.9}Ln_{0.05}Ag_{0.05}O_{2-\delta}$ composition (via EDS)	Crystallite size (nm)	Cell parameter (Å)
La_5Ag_5Ce	$Ce_{0.911}La_{0.053}Ag_{0.047}O_{1.925}$	63.1	5.434
Pr_5Ag_5Ce	$Ce_{0.892}Pr_{0.051}Ag_{0.051}O_{1.886}$	46.6	5.411
Nd_5Ag_5Ce	$Ce_{0.921}Nd_{0.049}Ag_{0.050}O_{1.940}$	32.3	5.417
Sm_5Ag_5Ce	$Ce_{0.896}Sm_{0.048}Ag_{0.053}O_{1.890}$	60.2	5.421
Gd_5Ag_5Ce	$Ce_{0.889}Gd_{0.054}Ag_{0.050}O_{1.884}$	39.4	5.389
Tb_5Ag_5Ce	$Ce_{0.905}Tb_{0.051}Ag_{0.046}O_{1.909}$	41.3	5.410
Dy_5Ag_5Ce	$Ce_{0.910}Dy_{0.053}Ag_{0.048}O_{1.923}$	61.5	5.411
Er_5Ag_5Ce	$Ce_{0.899}Er_{0.050}Ag_{0.055}O_{1.900}$	38.1	5.411

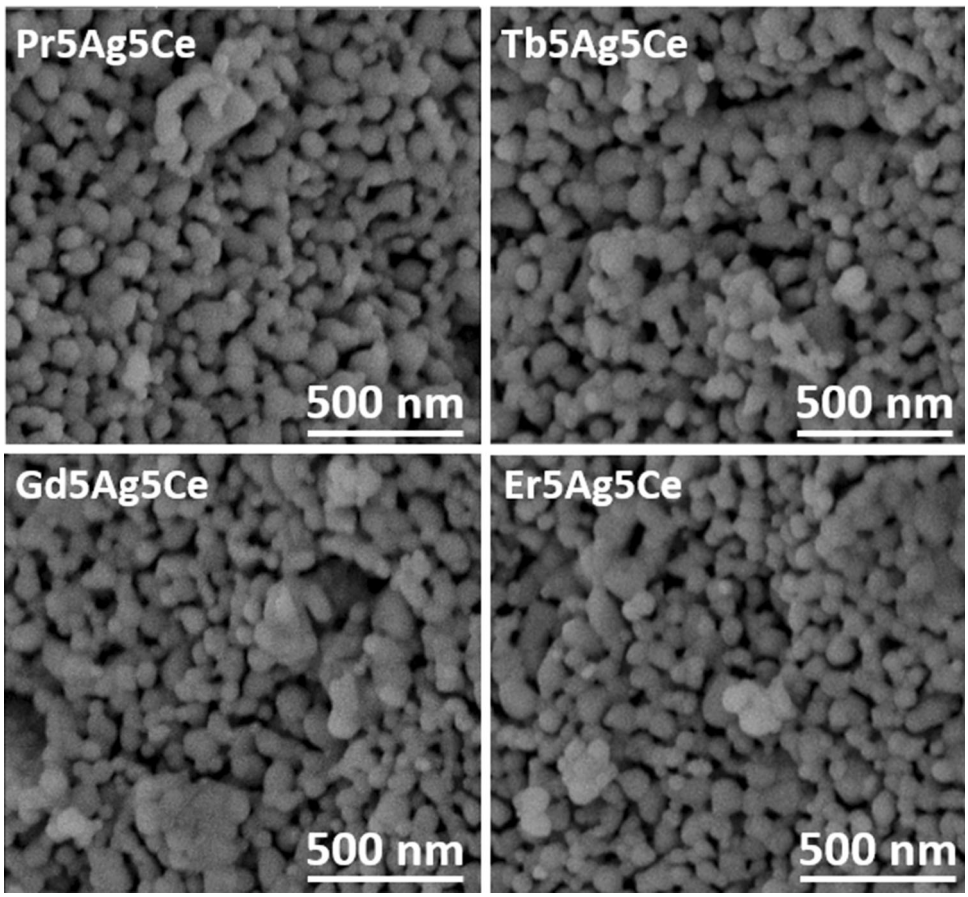

Figure 5 SEM images of Pr_5Ag_5Ce, Tb_5Ag_5Ce, Gd_5Ag_5Ce, and Er_5Ag_5Ce.

Nd_5Ag_5Ce was better than the other $Ce_{0.9}Ln_{0.05}Ag_{0.05}O_{2-\delta}$ materials.

Interesting to note that the n_{CO} produced by each $Ce_{0.9}Ln_{0.05}Ag_{0.05}O_{2-\delta}$ material was considerably lower than the n_{O_2} released during the first cycle. The two probable reasons for these results are (a) poor re-oxidation ability of the $Ce_{0.9}Ln_{0.05}Ag_{0.05}O_{2-\delta}$ materials or (b) additional mass loss during the first TR reduction due to the release of volatile chemicals from the $Ce_{0.9}Ln_{0.05}Ag_{0.05}O_{2-\delta}$ materials (which remained unburnt during the calcination step). For further investigation of this matter, the $Ce_{0.9}Ln_{0.05}Ag_{0.05}O_{2-\delta}$ materials were tested for three cycles (by maintaining the same operating conditions utilized in

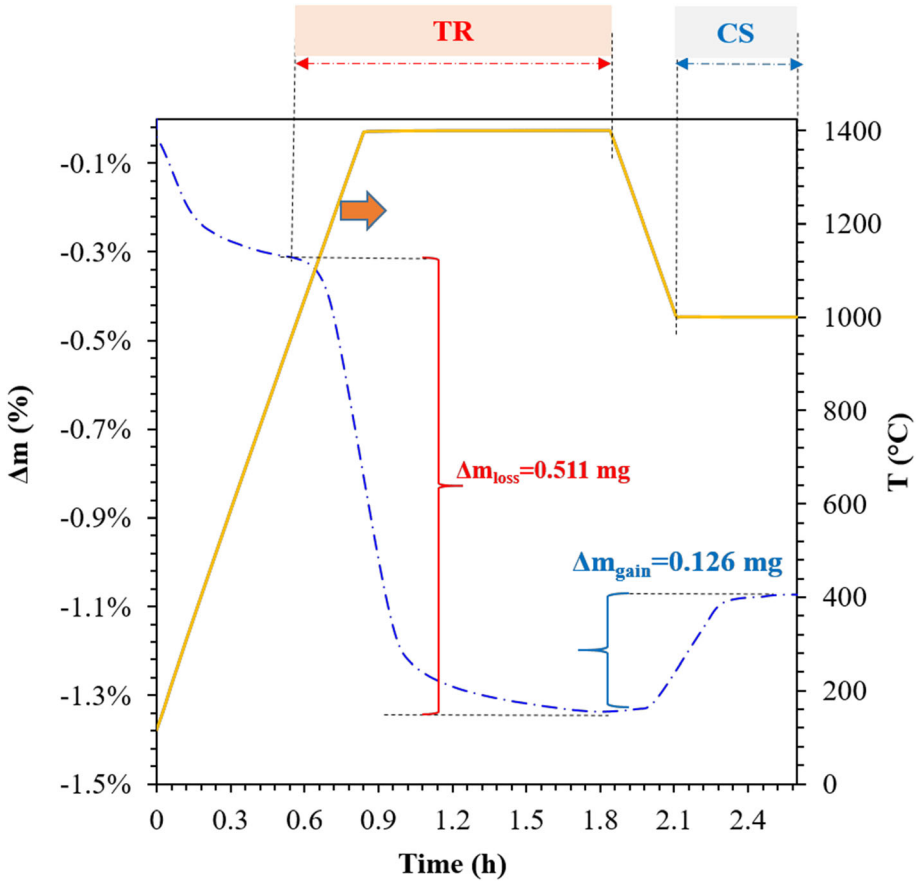

Figure 6 Exemplified TGA profile of La_5Ag_5Ce material during the first CDS cycle.

the case of the first cycle). Figure 8 shows the variations in the mass of the $Ce_{0.9}Ln_{0.05}Ag_{0.05}O_{2-\delta}$ materials during the successive three thermochemical cycles. Besides, Fig. 9a and b compares the n_{O_2} released and n_{CO} produced by each $Ce_{0.9}Ln_{0.05}Ag_{0.05}O_{2-\delta}$ material from cycle 1 to cycle 3.

Figures 8 and 9 show that the n_{O_2} released by all the $Ce_{0.9}Ln_{0.05}Ag_{0.05}O_{2-\delta}$ materials during cycle 1 was considerably higher than cycle 2. For example, the n_{O_2} released by La_5Ag_5Ce, Nd_5Ag_5Ce, Gd_5Ag_5Ce, and Dy_5Ag_5Ce in cycle 2 was lower by 77.9%, 64.6%, 76.6%, and 80.0% as compared to cycle 1. The comparison between cycle 2 and cycle 3 shows a different story. The n_{O_2} released by all the $Ce_{0.9}Ln_{0.05}Ag_{0.05}O_{2-\delta}$ materials in cycle 3 was slightly less when compared to cycle 2. For instance, the n_{O_2} released by La_5Ag_5Ce, Nd_5Ag_5Ce, Gd_5Ag_5Ce, and Dy_5Ag_5Ce in cycle 3 was lower by 2.0%, 0.0%, 14.8%, and 1.8% than cycle 2. Based on the results given in Figs. 8 and 9, it can be concluded that the prime reason for the more substantial O_2 evolution in cycle 1 was the additional loss in the mass of the $Ce_{0.9}Ln_{0.05}Ag_{0.05}O_{2-\delta}$ materials due to the release of volatile chemicals.

In the case of the CDS step, the n_{CO} produced by each $Ce_{0.9}Ln_{0.05}Ag_{0.05}O_{2-\delta}$ material first decreased in cycle 2 (compared to cycle 1) and remained approximately stable in cycle 3 (compared to cycle 2). For example, the n_{CO} produced by La_5Ag_5Ce, Nd_5Ag_5Ce, Gd_5Ag_5Ce, and Dy_5Ag_5Ce in cycle 2 was 11.1%, 20.0%, 7.4%, and 24.5% lower than cycle 1. In contrast, the %decrease in the n_{CO} produced by La_5Ag_5Ce, Nd_5Ag_5Ce, Gd_5Ag_5Ce, and Dy_5Ag_5Ce in cycle 3 was dropped to 1.1%, 0.5%, 0.9%, and 1.2% when compared with the cycle 2 data. The n_{CO}/n_{O_2} ratio of all the $Ce_{0.9}Ln_{0.05}Ag_{0.05}O_{2-\delta}$ materials increased significantly in cycle 2 when compared with cycle 1. For instance, the n_{CO}/n_{O_2} ratio of La_5Ag_5Ce, Nd_5Ag_5Ce,

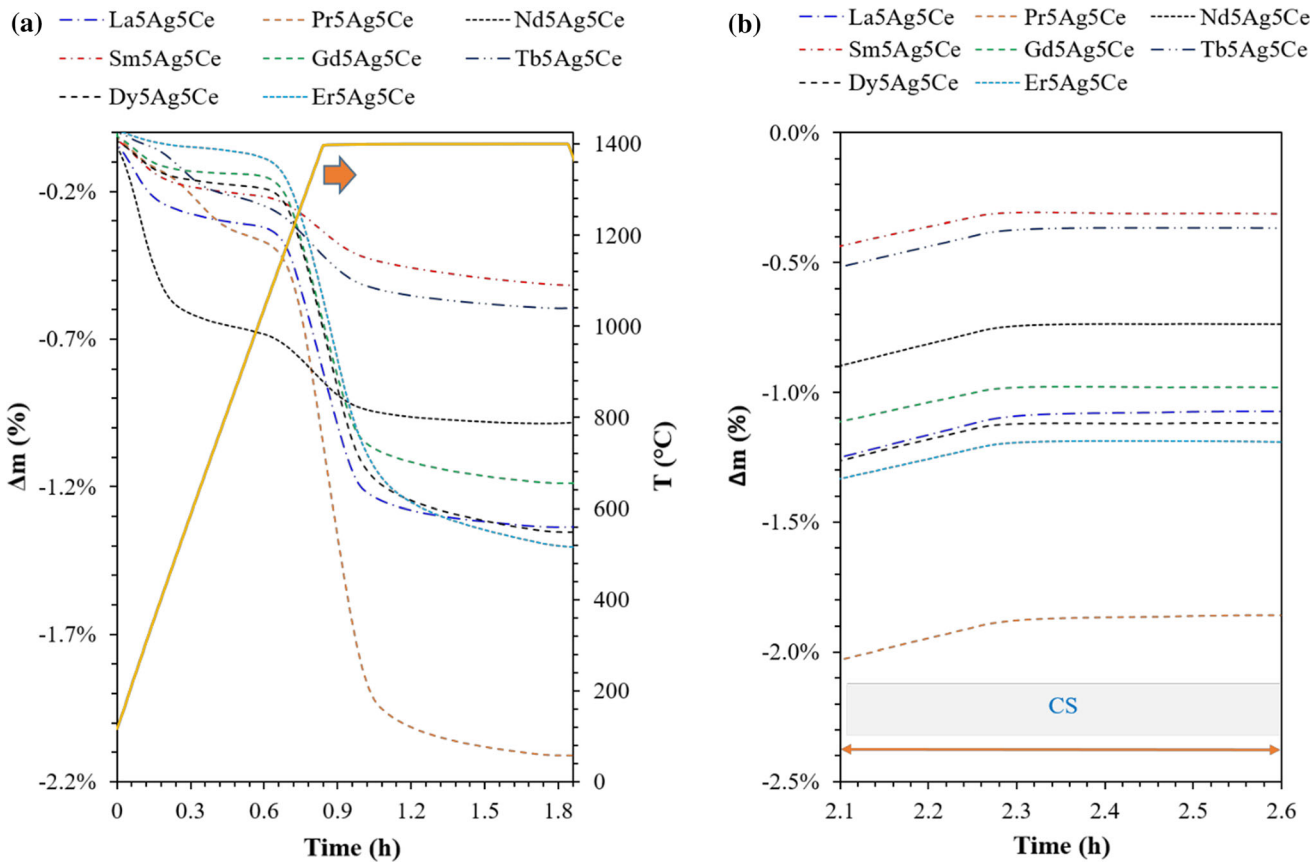

Figure 7 TGA profiles obtained for $Ce_{0.9}Ln_{0.05}Ag_{0.05}O_{2-\delta}$ materials during **a** first TR step and **b** first CDS step.

Table 3 Redox performance of $Ce_{0.9}Ln_{0.05}Ag_{0.05}O_{2-\delta}$ materials during the first cycle

$Ce_{0.9}Ln_{0.05}Ag_{0.05}O_{2-\delta}$	n_{O_2} released (μmol/g)	n_{CO} produced (μmol/g)	n_{CO}/n_{O_2} ratio
La_5Ag_5Ce	320.0	157.8	0.49
Pr_5Ag_5Ce	548.6	152.7	0.28
Nd_5Ag_5Ce	191.0	153.5	0.80
Sm_5Ag_5Ce	195.3	125.9	0.64
Gd_5Ag_5Ce	326.5	125.0	0.38
Tb_5Ag_5Ce	212.3	139.7	0.66
Dy_5Ag_5Ce	365.8	143.9	0.39
Er_5Ag_5Ce	415.4	134.1	0.32

Gd_5Ag_5Ce, and Dy_5Ag_5Ce increased by 1.49, 1.01, 1.13, and 1.09 in cycle 2 when compared with cycle 1. The n_{CO}/n_{O_2} ratio of all the $Ce_{0.9}Ln_{0.05}Ag_{0.05}O_{2-\delta}$ materials in cycle 2 and cycle 3 were almost identical.

The results obtained during cycle 3 indicate that most of the $Ce_{0.9}Ln_{0.05}Ag_{0.05}O_{2-\delta}$ materials are moving toward achieving a stable redox reactivity. For attaining further confirmation about the stable redox reactivity, the $Ce_{0.9}Ln_{0.05}Ag_{0.05}O_{2-\delta}$ materials were tested for ten successive cycles. The TGA profiles associated with the ten cycles are shown in Fig. 10. It was already confirmed that the data obtained in cycle 1 is misleading, and hence the TGA analysis was more focused on the remaining nine cycles. The n_{O_2}

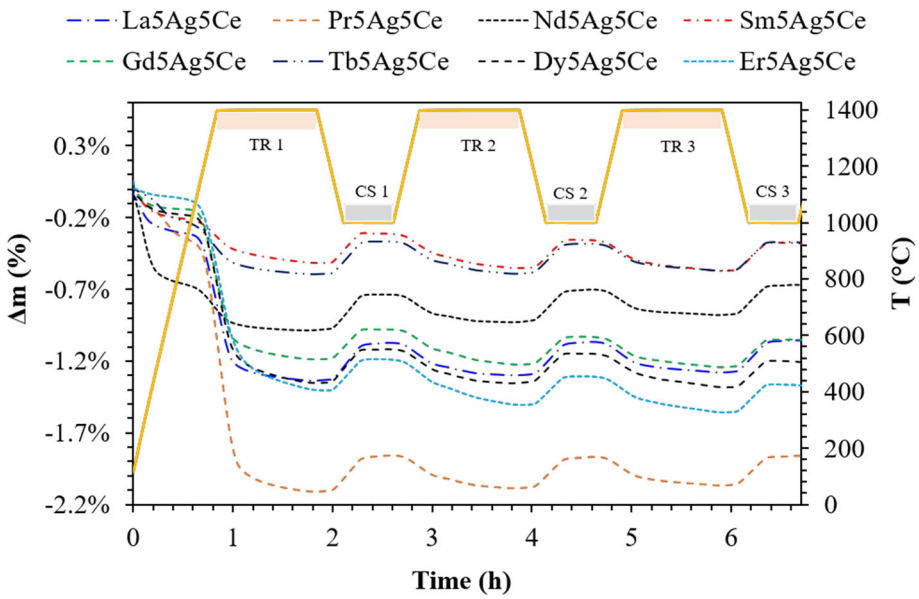

Figure 8 TGA profiles obtained for $Ce_{0.9}Ln_{0.05}Ag_{0.05}O_{2-\delta}$ materials during three cycles.

released and n_{CO} produced by each $Ce_{0.9}Ln_{0.05}Ag_{0.05}O_{2-\delta}$ material from cycle 2 to cycle 10 are shown in Figs. 11 and 12.

As per the data given in Fig. 11, the La_5Ag_5Ce, Pr_5Ag_5Ce, and Nd_5Ag_5Ce shows a stable release of O_2 from cycle 2 to cycle 10. The Gd_5Ag_5Ce indicates redox stability in terms of constant O_2 release from cycle 3 to cycle 10. For the rest of the $Ce_{0.9}Ln_{0.05}Ag_{0.05}O_{2-\delta}$ materials, i.e., Sm_5Ag_5Ce, Tb_5Ag_5Ce, Dy_5Ag_5Ce, and Er_5Ag_5Ce, a steady n_{O_2} evolution was realized after cycle 5 or cycle 6. In terms of average n_{O_2} released from cycle 2 to cycle 10, La_5Ag_5Ce (72.2 µmol of O_2/g cycle) and Tb_5Ag_5Ce (60.2 µmol of O_2/g cycle) were observed to be the best and worst among all the $Ce_{0.9}Ln_{0.05}Ag_{0.05}O_{2-\delta}$ materials.

As shown in Fig. 12, the La_5Ag_5Ce, Pr_5Ag_5Ce, Nd_5Ag_5Ce, Gd_5Ag_5Ce, and Dy_5Ag_5Ce showed a stable production of CO from cycle 2 to cycle 10. In contrast, a constant n_{CO} production in the case of Sm_5Ag_5Ce, Tb_5Ag_5Ce, and Er_5Ag_5Ce was noticed from cycle 6 to cycle 10. In terms of the average n_{CO} produced from cycle 2 to cycle 10, the $Ce_{0.9}Ln_{0.05}Ag_{0.05}O_{2-\delta}$ materials can be arranged as: $La_5Ag_5Ce > Nd_5Ag_5Ce \sim Pr_5Ag_5Ce > Gd_5Ag_5Ce > Tb_5Ag_5Ce > Sm_5Ag_5Ce \sim Er_5Ag_5Ce > Dy_5Ag_5Ce$.

According to the data given in Fig. 13, the re-oxidation ability (average n_{CO} / n_{O_2} ratio) of the La_5Ag_5Ce and Tb_5Ag_5Ce was the highest as compared to the rest of the $Ce_{0.9}Ln_{0.05}Ag_{0.05}O_{2-\delta}$ materials. Based on n_{O_2} released and n_{CO} produced from cycle 2 to cycle 10, the La_5Ag_5Ce appears to be the most excellent candidate among all the $Ce_{0.9}Ln_{0.05}Ag_{0.05}O_{2-\delta}$ materials investigated in this study.

Table 4 reports the comparison of $Ce_{0.9}Ln_{0.05}Ag_{0.05}O_{2-\delta}$ materials with the CeO_2 and $Ce_{0.9}Ln_{0.1}O_2$ materials. The results given in Table 4 shows that all the $Ce_{0.9}Ln_{0.05}Ag_{0.05}O_{2-\delta}$ materials were capable of higher n_{O_2} release (except for Sm_5Ag_5Ce) and n_{CO} production than CeO_2 and their corresponding $Ce_{0.9}Ln_{0.1}O_2$ materials. For instance, the n_{O_2} released by La_5Ag_5Ce, Pr_5Ag_5Ce, Nd_5Ag_5Ce, Gd_5Ag_5Ce, Tb_5Ag_5Ce, Dy_5Ag_5Ce, and Er_5Ag_5Ce was higher by 21.8 µmol of O_2/g cycle, 23.1 µmol of O_2/g cycle, 23.0 µmol of O_2/g cycle, 18.6 µmol of O_2/g cycle, 0.20 µmol of O_2/g cycle, 12.1 µmol of O_2/g cycle, and 8.50 µmol of O_2/g cycle as compared to $Ce_{0.9}La_{0.1}O_2$, $Ce_{0.9}Pr_{0.1}O_2$, $Ce_{0.9}Nd_{0.1}O_2$, $Ce_{0.9}Gd_{0.1}O_2$, $Ce_{0.9}Tb_{0.1}O_2$, $Ce_{0.9}Dy_{0.1}O_2$, and $Ce_{0.9}Er_{0.1}O_2$, respectively. Similarly, the La_5Ag_5Ce, Pr_5Ag_5Ce, Nd_5Ag_5Ce, Sm_5Ag_5Ce, Gd_5Ag_5Ce, Tb_5Ag_5Ce, Dy_5Ag_5Ce, and

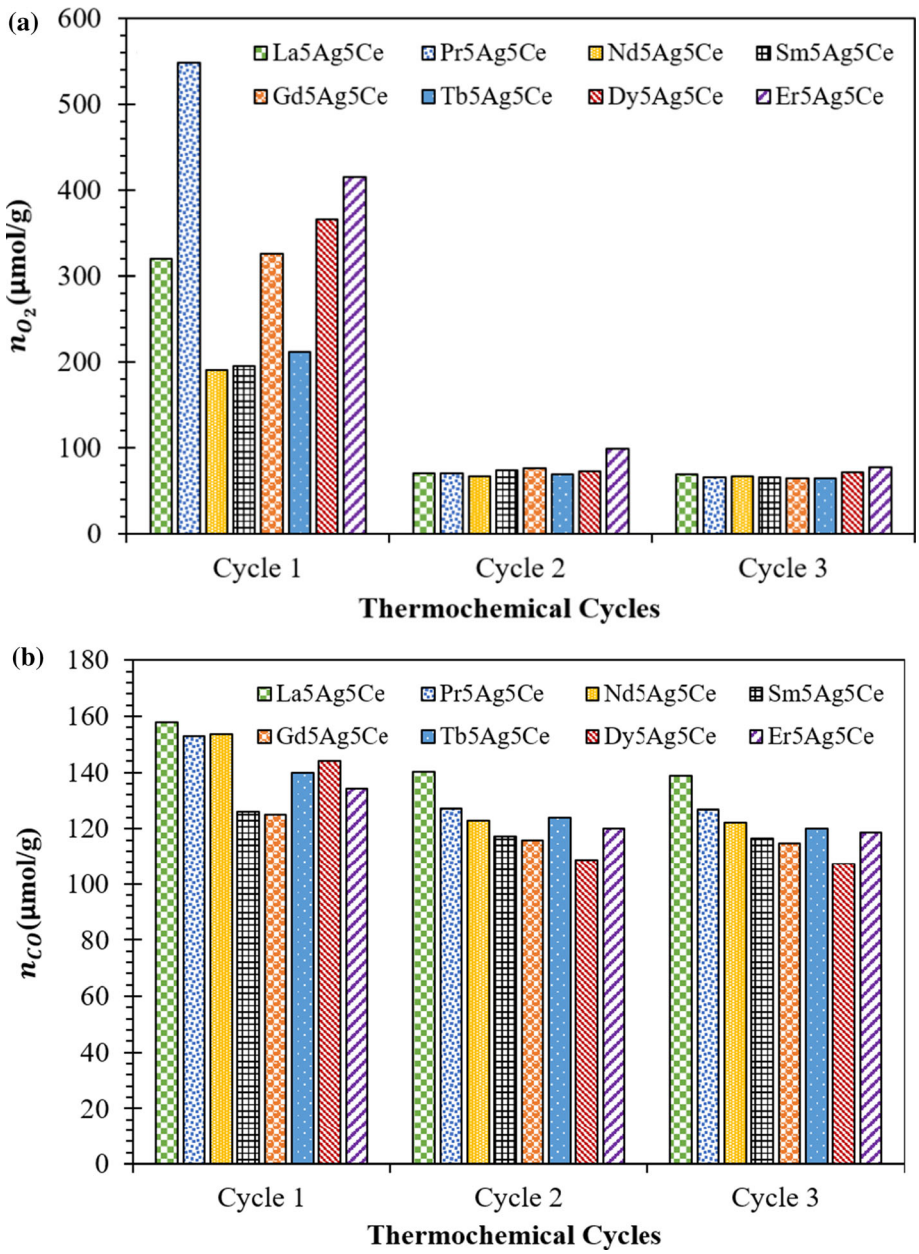

Figure 9 **a** n_{O_2} released and **b** n_{CO} produced by $Ce_{0.9}Ln_{0.05}Ag_{0.05}O_{2-\delta}$ materials during three cycles.

Er_5Ag_5Ce produced 1.39, 1.44, 1.52, 1.32, 1.49, 1.43, 1.29, and 1.37 times higher CO when compared with the $Ce_{0.9}La_{0.1}O_2$, $Ce_{0.9}Pr_{0.1}O_2$, $Ce_{0.9}Nd_{0.1}O_2$, $Ce_{0.9}Sm_{0.1}O_2$, $Ce_{0.9}Gd_{0.1}O_2$, $Ce_{0.9}Tb_{0.1}O_2$, $Ce_{0.9}Dy_{0.1}O_2$, and $Ce_{0.9}Er_{0.1}O_2$, respectively. The overall results of this investigation indicate that the incorporation of Ag in the Ln-doped ceria was beneficial to improve the redox performance of $Ce_{0.9}Ln_{0.05}Ag_{0.05}O_{2-\delta}$ materials.

Summary and conclusions

The PXRD and EDS analysis have confirmed the formation of nominally phase pure $Ce_{0.9}Ln_{0.05}Ag_{0.05}O_{2-\delta}$ materials via co-precipitation of the hydroxide method. The average crystallite size of the derived $Ce_{0.9}Ln_{0.05}Ag_{0.05}O_{2-\delta}$ materials was in the range of 32–64 nm. The SEM analysis further established a

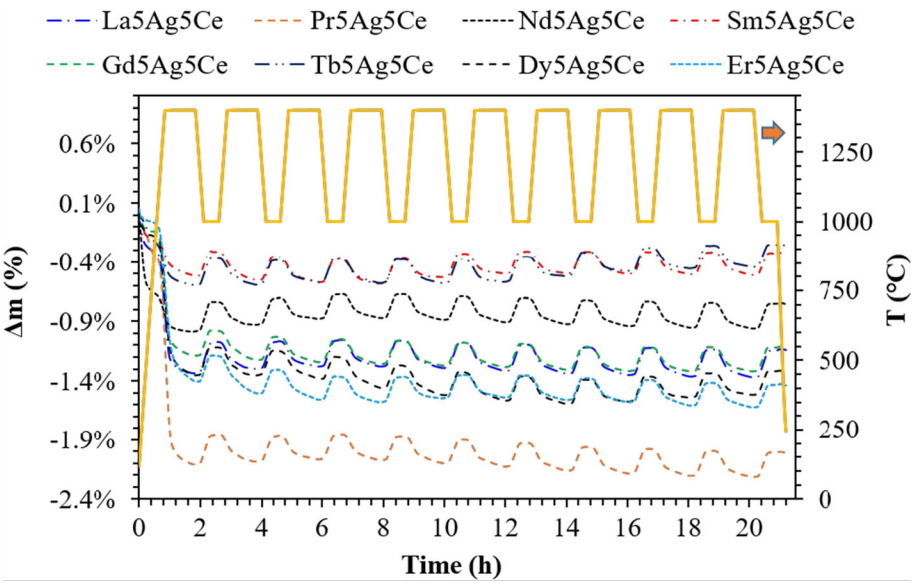

Figure 10 TGA profiles obtained during ten successive cycles performed using $Ce_{0.9}Ln_{0.05}Ag_{0.05}O_{2-\delta}$ materials.

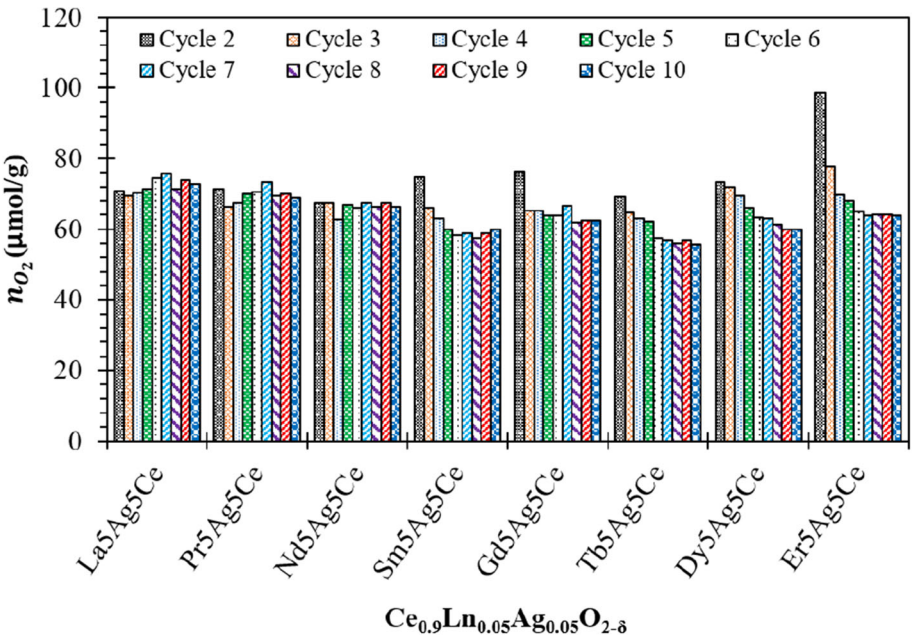

Figure 11 n_{O_2} released by $Ce_{0.9}Ln_{0.05}Ag_{0.05}O_{2-\delta}$ materials during ten successive cycles.

spherical nanostructured particle morphology of the $Ce_{0.9}Ln_{0.05}Ag_{0.05}O_{2-\delta}$ materials. The SEM analysis also indicates that the doping of the lanthanides and silver does not have any significant effect on the morphology of $Ce_{0.9}Ln_{0.05}Ag_{0.05}O_{2-\delta}$ materials. Based on the results associated with the TGA analysis, the redox reactivity of the $Ce_{0.9}Ln_{0.05}Ag_{0.05}O_{2-\delta}$ materials can be ranked as: $Ce_{0.911}La_{0.053}Ag_{0.047}O_{1.925}$ > $Ce_{0.921}Nd_{0.049}Ag_{0.050}O_{1.940}$ ~ $Ce_{0.892}Pr_{0.051}Ag_{0.051}O_{1.886}$ > $Ce_{0.889}Gd_{0.054}Ag_{0.050}O_{1.884}$ > $Ce_{0.905}Tb_{0.051}$

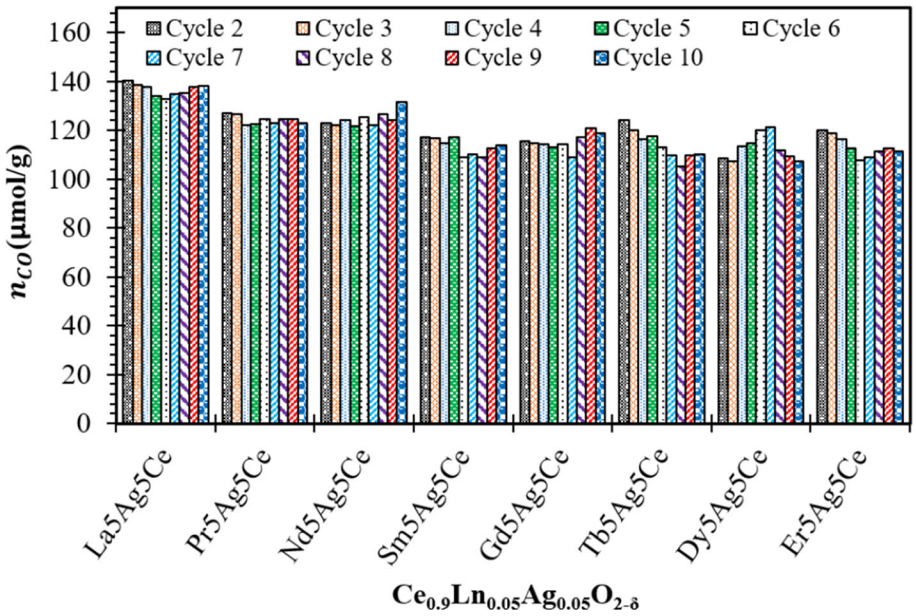

Figure 12 n_{CO} produced by $Ce_{0.9}Ln_{0.05}Ag_{0.05}O_{2-\delta}$ materials during ten successive cycles.

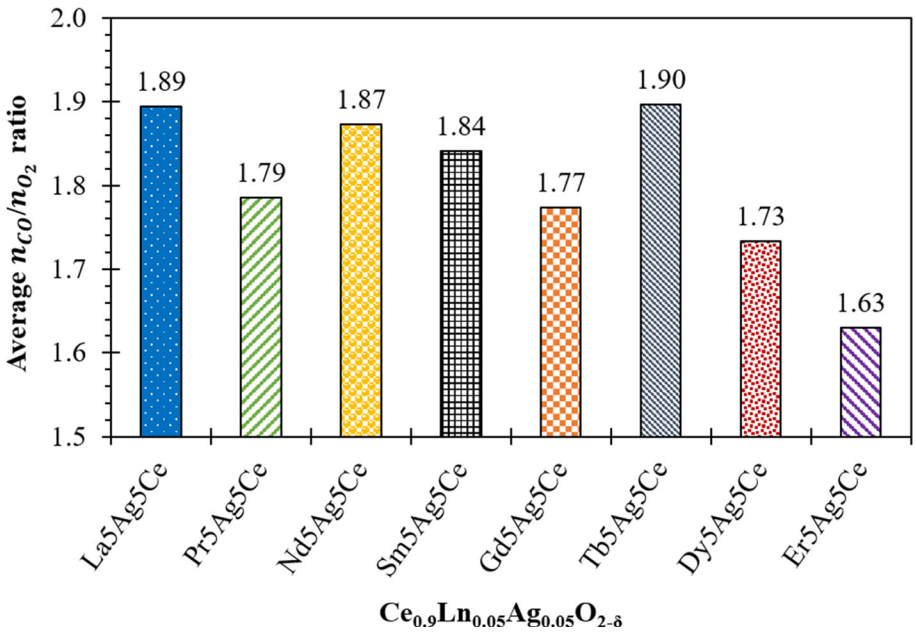

Figure 13 Average $^{n_{CO}}/_{n_{O_2}}$ ratio of the $Ce_{0.9}Ln_{0.05}Ag_{0.05}O_{2-\delta}$ materials.

$Ag_{0.046}O_{1.909}$ > $Ce_{0.896}Sm_{0.048}Ag_{0.053}O_{1.890}$ ~ $Ce_{0.899}Er_{0.050}Ag_{0.055}O_{1.900}$ > $Ce_{0.910}Dy_{0.053}Ag_{0.048}O_{1.923}$. The TGA results also indicate that the $Ce_{0.911}La_{0.053}Ag_{0.047}O_{1.925}$ and $Ce_{0.905}Tb_{0.051}Ag_{0.046}O_{1.909}$ possess the highest re-oxidation ability as compared to the rest of the $Ce_{0.9}Ln_{0.05}Ag_{0.05}O_{2-\delta}$ materials. The overall results of this investigation indicate that the inclusion of Ag into the Ln-doped ceria considerably improved the O_2 releasing and CO production capability of the $Ce_{0.9}Ln_{0.05}Ag_{0.05}O_{2-\delta}$ materials as compared to the phase pure CeO_2 and $Ce_{0.9}Ln_{0.1}O_2$ materials. After estimating the CO production capacity, our research team is currently focused on the production of H_2 by using the $Ce_{0.9}Ln_{0.05}Ag_{0.05}O_{2-\delta}$ materials.

Table 4 Comparison between the pure $CeO_{2-\delta}$, $Ce_{0.9}Ln_{0.1}O_{2-\delta}$, and $Ce_{0.9}Ln_{0.05}Ag_{0.05}O_{2-\delta}$ [19,33]

Materials	n_{O_2} released (μmol/g cycle)	n_{CO} produced (μmol/g cycle)
CeO_2	47.7	94.9
La_5Ag_5Ce	72.2	136.6
$Ce_{0.9}La_{0.1}O_2$	50.4	98.0
Pr_5Ag_5Ce	69.7	124.3
$Ce_{0.9}Pr_{0.1}O_2$	46.6	86.2
Nd_5Ag_5Ce	66.5	124.5
$Ce_{0.9}Nd_{0.1}O_2$	43.5	82.1
Sm_5Ag_5Ce	61.8	113.3
$Ce_{0.9}Sm_{0.1}O_2$	69.9	85.8
Gd_5Ag_5Ce	65.3	115.4
$Ce_{0.9}Gd_{0.1}O_2$	46.7	77.2
Tb_5Ag_5Ce	60.2	114.0
$Ce_{0.9}Tb_{0.1}O_2$	60.0	80.0
Dy_5Ag_5Ce	65.3	112.6
$Ce_{0.9}Dy_{0.1}O_2$	53.2	87.3
Er_5Ag_5Ce	70.5	113.3
$Ce_{0.9}Er_{0.1}O_2$	62.0	82.5

Acknowledgments

Open Access funding provided by the Qatar National Library. This publication was made possible by the NPRP Grant (NPRP8-370-2-154) from the Qatar National Research Fund (a member of Qatar Foundation). The statements made herein are solely the responsibility of author(s). The authors also gratefully acknowledge the Center of Advances Materials (CAM) at Qatar University for carrying out XRD analysis and the Central Laboratory Unit (CLU) for services related to scanning electron microscopy.

Compliance with ethical standards

Conflict of interest The authors declare that they have no conflict of interest.

References

[1] Varghese OK, Paulose M, LaTempa TJ, Grimes CA (2009) High-rate solar photocatalytic conversion of CO_2 and water vapor to hydrocarbon fuels. Nano Lett 9:731–737

[2] Patil GN, Vaidya PD, Kenig EY (2011) Reaction kinetics of CO_2 in aqueous methyl-and dimethylmonoethanolamine solutions. Ind Eng Chem Res 51:1592–1600

[3] Bhosale RR, Mahajani VV (2013) Kinetics of thermal degradation of renewably prepared amines useful for flue gas treatment. J Renew Sustain Energy 5:063110

[4] Anderson TR, Hawkins E, Jones PD (2016) CO2, the greenhouse effect and global warming: from the pioneering work of Arrhenius and Callendar to today's Earth System Models. Endeavour 40:178–187

[5] Carrillo RJ, Scheffe JR (2017) Advances and trends in redox materials for solar thermochemical fuel production. Sol Energy 156:3–20

[6] Koepf E, Alxneit I, Wieckert C, Meier A (2017) A review of high temperature solar driven reactor technology: 25 years of experience in research and development at the Paul Scherrer Institute. Appl Energy 188:620–651

[7] Dry ME (2002) The fischer–tropsch process: 1950–2000. Catal Today 71:227–241

[8] Bhosale RR (2018) Thermodynamic efficiency analysis of zinc oxide based solar driven thermochemical H_2O splitting cycle: effect of partial pressure of O_2, thermal reduction and H_2O splitting temperatures. Int J Hydrog Energy 43:14915–14924

[9] Abanades S, Charvin P, Flamant G (2007) Design and simulation of a solar chemical reactor for the thermal reduction of metal oxides: case study of zinc oxide dissociation. Chem Eng Sci 62:6323–6333

[10] Bhosale RR, Kumar A, Sutar P (2017) Thermodynamic analysis of solar driven SnO_2/SnO based thermochemical water splitting cycle. Energy Convers Manag 135:226–235

[11] Chambon M, Abanades S, Flamant G (2011) Thermal dissociation of compressed ZnO and SnO_2 powders in a moving-front solar thermochemical reactor. AIChE J 57:2264–2273

[12] Scheffe JR et al (2011) Hydrogen production via chemical looping redox cycles using atomic layer deposition-synthesized iron oxide and cobalt ferrites. Chem Mater 23:2030–2038

[13] Cho WC et al (2012) Reactivity of iron oxide as an oxygen carrier for chemical-looping hydrogen production. Int J Hydrog Energy 37:16852–16863

[14] Chueh WC, Haile SM (2010) A thermochemical study of ceria: exploiting an old material for new modes of energy conversion and CO_2 mitigation. Philos Trans A Math Phys Eng Sci 368:3269–3294

[15] Bhosale RR et al (2019) A decade of ceria based solar thermochemical H_2O/CO_2 splitting cycle. Int J Hydrog Energy 44:34–60

[16] Ackermann S, Scheffe JR, Steinfeld A (2014) Diffusion of oxygen in ceria at elevated temperatures and its application to H_2O/CO_2 splitting thermochemical redox cycles. J Phys Chem C 118:5216–5225

[17] Scheffe JR, Jacot R, Patzke GR, Steinfeld A (2013) Synthesis, characterization, and thermochemical redox performance of Hf4, Zr4, and Sc3 doped ceria for splitting CO_2. J Phys Chem C 117:24104–24114

[18] Le Gal A, Abanades S (2011) Catalytic investigation of ceria-zirconia solid solutions for solar hydrogen production. Int J Hydrog Energy 36:4739–4748

[19] Takalkar G et al (2018) Transition metal doped ceria for solar thermochemical fuel production. Sol Energy 172:204–211

[20] Muhich CL et al (2013) Efficient generation of H_2 by splitting water with an isothermal redox cycle. Science 341:540–542

[21] Shende RV, Puszynski JA, Opoku MK, Bhosale RR (2009) Synthesis of novel ferrite foam material for water-splitting application. In: Proceedings of NSTIdNanotech conference & expo., ISBN, 2009

[22] Bhosale RR, Shende RV, Puszynski JA (2012) Sol-gel derived $NiFe_2O_4$ modified with ZrO_2 for hydrogen generation from solar thermochemical water-splitting reaction. In: MRS online proceedings library archive, vol 1387

[23] Agrafiotis C, Zygogianni A, Pagkoura C, Kostoglou M, Konstandopoulos AG (2013) Hydrogen production via solar-aided water splitting thermochemical cycles with nickel ferrite: experiments and modeling. AIChE J 59:1213–1225

[24] Scheffe JR, Li J, Weimer AW (2010) A spinel ferrite/hercynite water-splitting redox cycle. Int J Hydrog Energy 35:3333–3340

[25] Scheffe JR, Weibel D, Steinfeld A (2013) Lanthanum–strontium–manganese perovskites as redox materials for solar thermochemical splitting of H_2O and CO_2. Energy Fuels 27:4250–4257

[26] Dey S, Naidu B, Govindaraj A, Rao C (2015) Noteworthy performance of La_{1-x} Ca_x MnO_3 perovskites in generating H_2 and CO by the thermochemical splitting of H_2 O and CO_2. Phys Chem Chem Phys 17:122–125

[27] Bhosale RR et al (2017) La-based perovskites as oxygen-exchange redox materials for solar syngas production. MRS Adv 2:3365–3370

[28] Gálvez M et al (2015) Physico-chemical changes in Ca, Sr and Al-doped La–Mn–O perovskites upon thermochemical splitting of CO_2 via redox cycling. Phys Chem Chem Phys 17:6629–6634

[29] Bhosale RR, Kumar A, AlMomani F, Ghosh U, Khraisheh M (2017) A comparative thermodynamic analysis of samarium and erbium oxide based solar thermochemical water splitting cycles. Int J Hydrog Energy 42:23416–23426

[30] Bhosale R et al (2016) Solar hydrogen production via a samarium oxide-based thermochemical water splitting cycle. Energies 9:316

[31] Bhosale RR et al (2016) Solar hydrogen production via erbium oxide based thermochemical water splitting cycle. J Renew Sustain Energy 8:034702

[32] Bhosale R, Kumar A, AlMomani F (2016) Solar thermochemical hydrogen production via terbium oxide based redox reactions. Int J Photoenergy. https://doi.org/10.1155/2016/9727895

[33] Bhosale R, Takalkar G (2018) Nanostructured co-precipitated $Ce_{0.9}Ln_{0.1}O_2$ (Ln = La, Pr, Sm, Nd, Gd, Tb, Dy, or Er) for thermochemical conversion of CO_2. Ceram Int 44:16688–16697